RSC Advances

PAPER

View Article Online
View Journal | View Issue

Cite this: *RSC Adv.*, 2023, **13**, 33697

High-performance flexible strain sensors based on silver film wrinkles modulated by liquid PDMS substrates†

Yifan Xu,[a] Miaogen Chen,[a] Senjiang Yu*[b] and Hong Zhou[a]

Flexible strain sensors based on controllable surface microstructures in film-substrate systems can be extensively applied in high-tech fields such as human–machine interfaces, electronic skins, and soft robots. However, the rigid functional films are susceptible to structural destruction and interfacial failure under large strains or high loading speeds, limiting the stability and durability of the sensors. Here we report on a facile technique to prepare high-performance flexible strain sensors based on controllable wrinkles by depositing silver films on liquid polydimethylsiloxane (PDMS) substrates. The silver atoms can penetrate into the surface of liquid PDMS to form an interlocking layer during deposition, enhancing the interfacial adhesion greatly. After deposition, the liquid PDMS is spontaneously solidified to stabilize the film microstructures. The surface patterns are well modulated by changing film thickness, prepolymer-to-crosslinker ratio of liquid PDMS, and strain value. The flexible strain sensors based on the silver film/liquid PDMS system show high sensitivity (above 4000), wide sensing range (~80%), quick response speed (~80 ms), and good stability (above 6000 cycles), and have a broad application prospect in the fields of health monitoring and motion tracking.

Received 4th September 2023
Accepted 13th November 2023

DOI: 10.1039/d3ra06020a

rsc.li/rsc-advances

1. Introduction

With the rapid development of modern science and technology of the Internet of Things, wearable flexible electronics has been a research hotspot in the electronic and information industry.[1–4] Wearable flexible electronic devices can directly attach to human skin or put on as clothes. They have the advantages of lightness, thinness, flexibility and being comfortable, and can achieve various operation and monitoring applications such as health monitoring, motion tracking, and human–machine interaction.[5–10] As an important component of the wearable system, flexible strain sensors have been the main research direction for the development of future intelligent devices.[11–18]

The flexible strain sensors can be realized by depositing or coating functional units such as metal films,[19–22] conducting polymers,[10,13,15] and two-dimensional materials[23,24] on soft substrates. Due to the flexibility, bendability and stretchability of the soft substrates, the sensors can well fit to the non-planar human skins or other curved surfaces. The design of surface structures and film microstructures is extremely important to achieve high sensitivity and reliability of the flexible strain sensors.[25,26] For examples, Ji *et al.* have prepared the flexible strain sensors based on V-shaped substrate groove/film wrinkle hierarchical arrays and have achieved high sensitivity and a wide sensing range.[21] Xiao *et al.* have obtained the flexible strain sensors with high durability, quick response and high sensitivity based on ZnO nanowire/polystyrene hybridized films.[27]

Although various high performance flexible strain sensors have been realized by constructing the bilayer system comprising of a rigid functional film and a stretchable substrate, the reliability and durability of such system are still a big challenge. For the frequently-used flexible substrates such as polydimethylsiloxane (PDMS), silicone rubber (Ecoflex), and polyurethane (PU), the deposited or coated rigid films are susceptible to occurring interfacial failure and buckle delamination due to the extreme mechanical mismatch between films and substrates.[28,29] Furthermore, the plasticity or viscoelasticity behaviors of the substrates may induce the instability of film microstructures and lead to performance degradation of the sensors, especially in the situations of high loading frequency and high strain.[30] To solve or alleviate these issues, many strategies have been developed by changing film-substrate materials and designing specific structures.[31–33] Among these, controlling substrate modulus is a promising solution. Yu *et al.* showed that the metal films deposited on elasticity-gradient PDMS substrates form gradually varied surface patterns.[34] Liu

[a]*Key Laboratory of Intelligent Manufacturing Quality Big Data Tracing and Analysis of Zhejiang Province, College of Science, China Jiliang University, Hangzhou 310018, P.R. China. E-mail: phycmg@cjlu.edu.cn*

[b]*Key Laboratory of Novel Materials for Sensor of Zhejiang Province, College of Materials and Environmental Engineering, Hangzhou Dianzi University, Hangzhou 310018, P.R. China. E-mail: sjyu@hdu.edu.cn*

† Electronic supplementary information (ESI) available. See DOI: https://doi.org/10.1039/d3ra06020a

et al. reported that the gold film deposited on a semi-polymerized PDMS substrate forms an interlocking layer between PDMS and gold, leading to significant enhancement of the stability of stretchable conductors.[35]

Inspired by the previous researches on tunable surface and interfacial properties *via* substrate modulus, here we report on the high-performance flexible strain sensors based on silver film wrinkles modulated by liquid PDMS substrates. Through substrate prestretching, silver film deposition and subsequent prestrain releasing, periodic film wrinkles are achieved. The wrinkle wavelength and amplitude are controllable by changing film thickness, prepolymer-to-crosslinker ratio of liquid PDMS, and strain value. During film deposition, the silver atoms can penetrate into the surface of liquid PDMS to form an interlocking layer, improving the interfacial adhesion greatly. After film deposition, the liquid PDMS is spontaneously solidified to stabilize the film microstructures. The flexible strain sensors based on the silver film/liquid PDMS system possess high stability, high sensitivity, wide sensing range, and quick response speed. Owing to the high comprehensive performances, these flexible strain sensors can be applied for monitoring human motion signals.

2. Experimental section

2.1. Preparation of substrates

Fig. 1 shows the schematic illustration of sample preparation. The corresponding photographs of the sample during preparation are shown in Fig. S1 in the ESI.† The polydimethylsiloxane (PDMS, Sylgard-184, Dow Corning) was used as the flexible substrates in this study. The prepolymer and crosslinker with a mass ratio of 10 : 1 were mixed fully. After the mixture was placed on a horizontal table for half an hour to eliminate the bubbles completely, it was poured into a Petri dish with the diameter of 90 mm and the depth of 16 mm. Then the Petri dish was placed on a hot plate with 70 °C for 5 h to cure the PDMS completely. The solidified PDMS (with the thickness of about 1.2 mm) was cut into rectangular sheets with the size of 35×12 mm^2, as shown in Fig. 1(a). Then liquid PDMS mixtures with different prepolymer-to-crosslinker ratios (*e.g.*, 1 : 1, 2 : 1, 5 : 1, 10 : 1, 15 : 1, 20 : 1, 30 : 1 and 40 : 1) were spin-coated on the solidified PDMS sheets with the rotation speed of 4000 rpm and the rotation time of 30 s, as shown in Fig. 1(b). The thickness of liquid PDMS layers was about 20 μm.

2.2. Film deposition

The cured PDMS sheets with liquid PDMS atop were mounted on custom-designed uniaxial stretching devices and were stretched to a uniform prestrain of 30%, 50% or 70%, as shown in Fig. 1(c). Silver (Ag) films were deposited on the liquid PDMS surfaces by direct current magnetron sputtering at room temperature, as shown in Fig. 1(d). The sputtering power was 45 W (250 V voltage and 0.167 A current) and the argon gas pressure was 0.5 Pa. The deposition rate of Ag films was about 0.75 nm s^{-1}. The film thickness was controlled by changing the deposition time. During or after deposition, the liquid PDMS is spontaneously cured to form elastic polymer materials. Note that the magnetron sputtering technique has obvious advantages such as high film quality, homogeneity and strong interfacial adhesion compared with some chemical methods. The crystal structure of the Ag film was performed by an X-ray diffractometer (MinFlex600) and the Ag diffraction peaks can be seen clearly as shown in Fig. S2 in the ESI.†

2.3. Prestrain releasing

After deposition, the prestrain was released slowly and surface wrinkles formed, as shown in Fig. 1(e). The film strain can be calculated as $\varepsilon = \frac{L - L_0}{L_0}$, where L_0 and L were the initial and final film lengths, respectively. The maximum film strain was about −23.1% when the prestrain was released completely. The minus sign represented compressive strain. For simplicity, we used the absolute value of strain in this study.

2.4. Preparation of sensors

After prestrain releasing, silver foils were attached to the Ag film surfaces at two sides of the samples, serving as the conducting

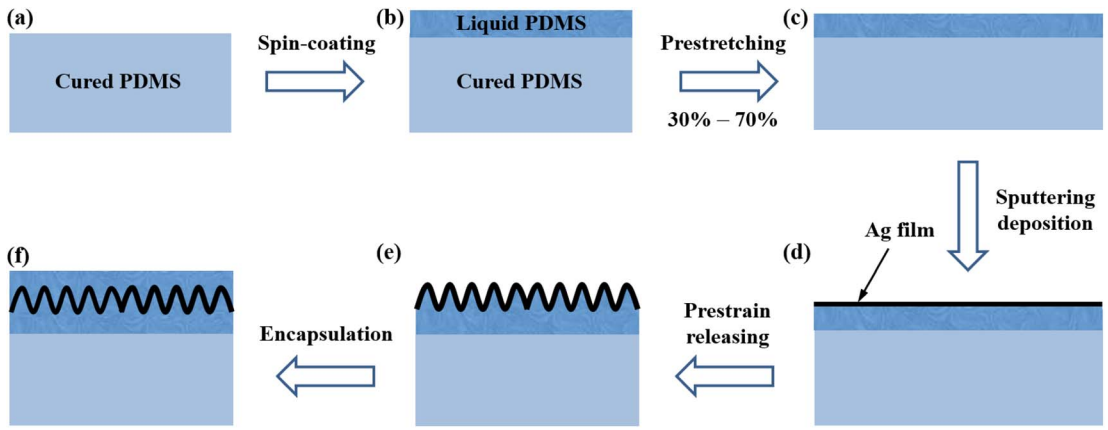

Fig. 1 Schematic illustration of sample preparation. The experimental procedure can be divided into six steps: preparation of a solidified PDMS sheet (a), spin-coating a liquid PDMS thin layer (b), uniaxial stretching (c), silver film deposition (d), prestrain releasing (e), and device encapsulation (f).

electrodes of the sensors. Then liquid PDMS with 20 : 1 mass ratio was spin-coated on the wrinkled Ag film surfaces (also on the electrodes) and then cured at 60 °C for 7 h, as shown in Fig. 1(f). The encapsulated samples had comparatively stable structures and properties.

2.5. Characterization

An optical microscope (Olympus BX41) was adopted to detect the surface morphologies. A stylus profiler (DektakXT, Bruker) was adopted to measure the surface profiles. An atomic force microscope (AFM, JPKSPM) operated in tapping mode was used to detect the three-dimensional features of wrinkle patterns. The samples were cut by a blade along the loading direction and the cross-sectional profiles were detected by the optical microscope. The electrical properties were measured and recorded by a multimeter (SDM3065X).

3. Results and discussion

3.1. Morphological features

Fig. 2(a–c) shows the surface morphology and profile of the Ag film ($h = 90$ nm) deposited on the liquid (uncured) PDMS (20 : 1) after prestrain releasing. For comparison, the surface morphology and profile of the Ag film with the same thickness on the solid (cured) PDMS with the same prepolymer-to-crosslinker ratio are shown in Fig. 2(d–f). We find that the Ag films on the liquid and solid PDMS both form periodical wrinkles perpendicular to the loading direction. Obviously, the wrinkle wavelength λ and amplitude A on the liquid PDMS are much larger than the values on the solid PDMS. The formation and evolution of the wrinkle patterns will be discussed in the next section in detail.

In the orthogonal direction, cracks form due to the Poisson's effect-induced lateral stretching (see the black linear structures parallel to the loading direction as shown in Fig. 2(d)).[28,36] The crack morphologies of Ag films on the solid and liquid PDMS substrates with different film thicknesses and prepolymer-to-crosslinker ratios are shown in Fig. S3 in the ESI.† The Ag film on the liquid PDMS possesses lesser cracks compared with that on the solid PDMS. On the contrary, the cracks on the liquid PDMS have larger widths compared with those on the solid PDMS, as shown in Fig. S4 in the ESI.† According to the fracture theory,[37,38] the cracks generate when the elastic strain energy exceeds the fracture energy of materials, *i.e.*, $2\gamma he \geq G_c h$ with $e = h\sigma^2(1 - \nu_f)/E_f$. Here h is the film thickness, σ is the tensile stress, G_c is the density of fracture energy (fracture toughness), E_f is the Young's modulus of film, γ is a dimensionless parameter, which is determined by fracture mode and mismatch between the film and substrate. Furthermore, the spacing of cracks can be expressed as[28,39]

$$d = \frac{2hG_c}{E_s(\varepsilon - \varepsilon_c)}, \quad (1)$$

where ε is the tensile strain, ε_c is the critical strain for crack generation, and E_s is the Young's modulus of substrate. In this study, the film thickness, fracture toughness and tensile strain are all constant. The crack spacing is inversely proportional to

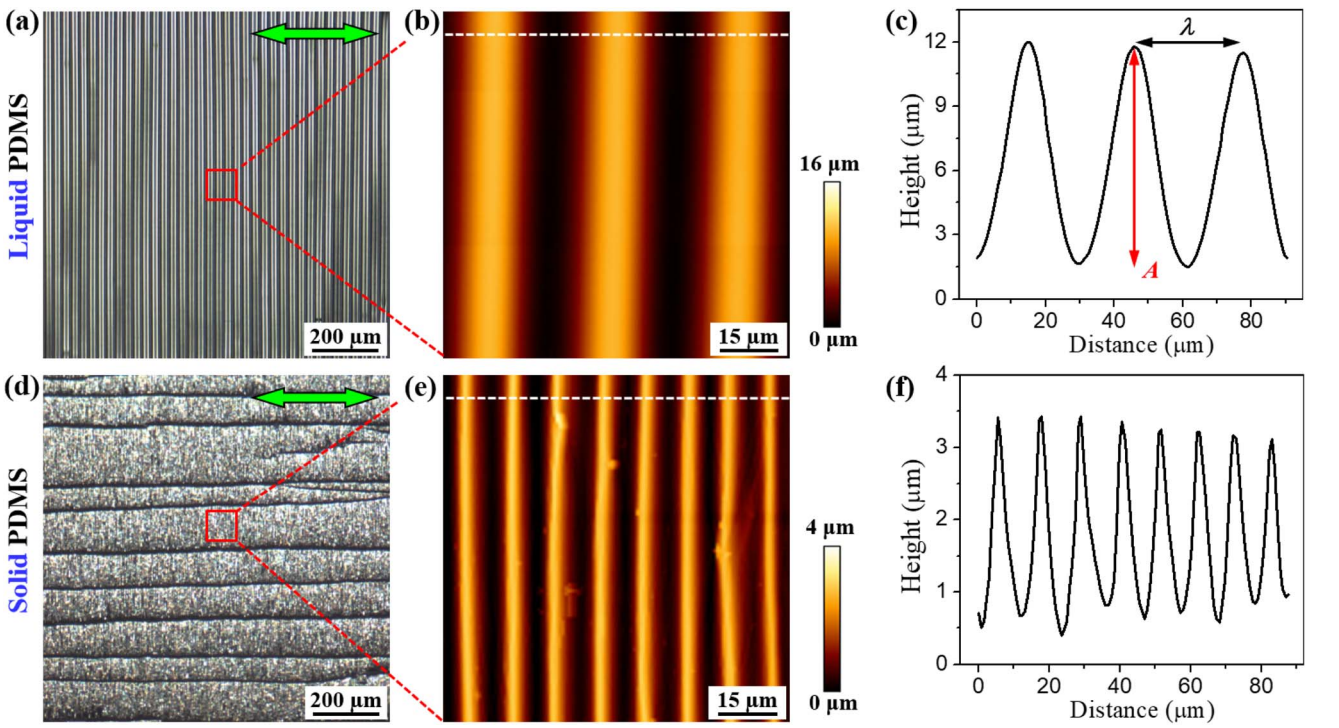

Fig. 2 Morphological comparison of silver films on the liquid (upper) and solid (lower) PDMS substrates (30% prestrain). (a and d) Optical micrographs. The bidirectional arrows represent the prestrain loading direction. (b and e) Atomic force microscope (AFM) images. (c and f) Corresponding AFM profiles.

the Young's modulus of substrate. The equivalent Young's modulus of the liquid PDMS is much smaller than that of the solid PDMS, leading to the lesser cracks on the liquid PDMS substrates. Furthermore, as the film thickness increases, the crack number decreases according to eqn (1), in good agreement with the experimental observations (see Fig. S4 in the ESI†).

3.2. *In situ* morphological evolution

Fig. 3(a) shows the *in situ* morphological evolution of the Ag film with $h = 90$ nm on the liquid PDMS substrate during the pre-strain releasing process. Fig. 3(b) shows the evolution of profiles taken by a stylus profiler. It is clear that the as-prepared Ag film is smooth and wrinkle-free. As a small compressive strain is exerted, periodical wrinkles perpendicular to the loading direction form. The wrinkles exhibit a regularly sinusoidal profile with a well-defined wavelength and amplitude. As the compressive strain increases, the wrinkles become more prominent and the wrinkle amplitude increases greatly. To further understand the morphological evolution of the Ag film/liquid PDMS system, we have measured the dependences of wrinkle wavelength λ and amplitude A on the compressive strain ε, as shown in Fig. 3(c and d). We find that the wrinkle wavelength decreases while the amplitude increases steadily with increasing compressive strain.

According to the continuous elastic theory, wrinkles form in the film-substrate system when the imposed compressive strain exceeds a critical value, which is expressed as[40]

$$\varepsilon_c = \frac{1}{4}\left[\frac{3E_s(1-\nu_f^2)}{E_f(1-\nu_s^2)}\right]^{2/3}, \quad (2)$$

where ν_f and ν_s are the Poisson's ratios of film and substrate, respectively. The critical wrinkling strain is determined by the material parameters of the film and substrate, and it is independent of the film thickness. For metal film/PDMS systems, the Young's modulus of film (~100 GPa) is 5 orders of magnitude larger than that of PDMS (~1 MPa). Therefore the critical wrinkling strain is very small for metal film/PDMS systems, which has been verified by a large number of previous studies.[40,41] The energy minimization of the film-substrate system leads to a balanced wrinkle configuration with the wavelength and amplitude expressed as[40,42]

$$\lambda_0 = 2\pi h\left[\frac{E_f(1-\nu_s^2)}{3E_s(1-\nu_f^2)}\right]^{1/3}. \quad (3)$$

$$A_0 = h\left(\frac{\varepsilon}{\varepsilon_c}-1\right)^{1/2}. \quad (4)$$

Note that the above equations are only suitable for small strain condition (approaching to the critical wrinkling strain). For large strain condition, the wrinkle wavelength and amplitude should be modified according to the finite deformation theory[43]

$$\lambda = \frac{\lambda_0}{(1+\varepsilon)(1+\xi)^{1/3}}, \quad (5)$$

$$A = \frac{A_0}{(1+\varepsilon)^{1/2}(1+\xi)^{1/3}}, \quad (6)$$

where $\xi = 5\varepsilon(1+\varepsilon)/32$. Fig. 3(c and d) shows that the theoretical predications based on eqn (5) and (6) are in good agreement with the experimental measurements.

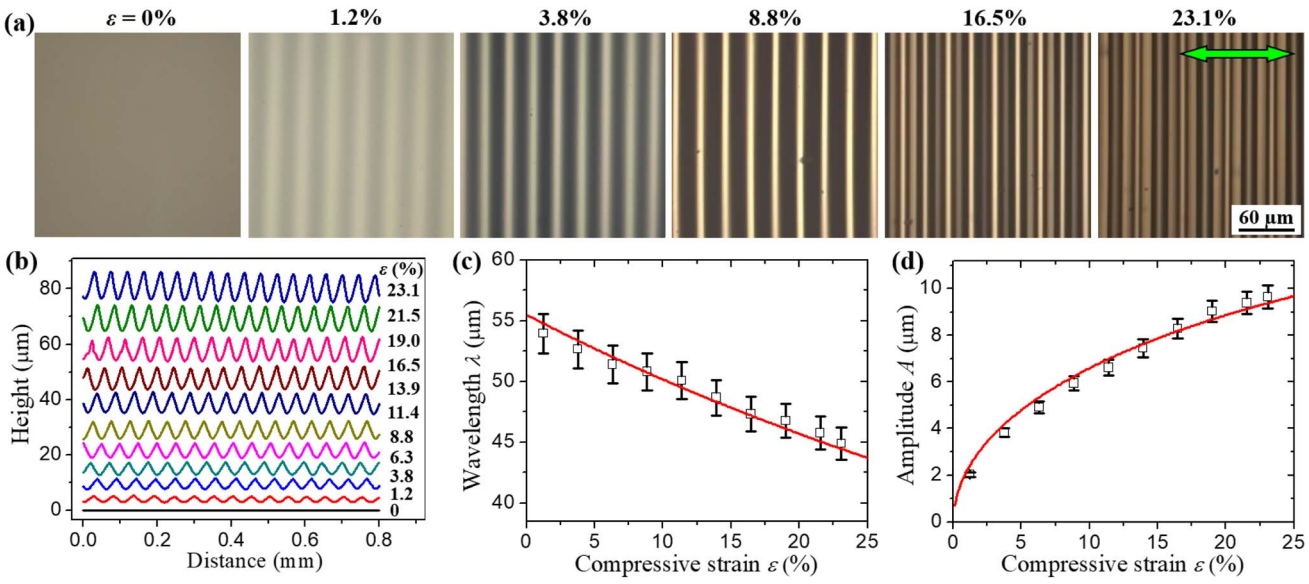

Fig. 3 (a) *In situ* morphological evolution of the silver film with $h = 90$ nm on the liquid PDMS substrate with prepolymer-to-crosslinker ratio of 20 : 1 by uniaxial compression. The data above the images represent the compressive strain. Each image has a size of 220 × 220 μm^2. (b) Wrinkle profiles under different compressive strains. (c and d) Evolutions of wrinkle wavelength λ (c) and amplitude A (d) with the compressive strain ε. The solid lines are fitted to the experimental data based on the finite deformation theory.

3.3. Dependence of film thickness

Fig. 4(a) shows the surface morphologies of Ag film/liquid PDMS systems with different film thicknesses after prestrain releasing. Fig. 4(b) shows the comparison of surface profiles for different film thicknesses. Our experiment shows that thicker Ag films usually generate buckle-delaminations during the strain loading as shown in Fig. S5 and S6 in the ESI.† For the samples with $h = 135$ and 225 nm, sinusoidal wrinkle profiles first form for small strains. When the compressive strain increases, the localized instability mode starts to appear and the wrinkles and buckle-delaminations coexist. The appearance of buckle-delaminations can suppress the wrinkles nearby and thus the wrinkle amplitude decreases (see Fig. S5 in the ESI†). For the sample with $h = 360$ nm, the wrinkles are almost disappeared and only buckle-delaminations exist when the strain is large enough (see Fig. S6 in the ESI†). The buckle-delaminations are originated from the weaker interface between the film and substrate. The coexistence and coevolution of wrinkles and buckle-delaminations have been extensively investigated in the previous studies.[44–47]

Fig. 4(c and d) shows the dependences of wavelengths and amplitudes of wrinkles and buckle-delaminations on the film thickness. We find that the wrinkle wavelength increases approximately linearly with the film thickness. The delamination width is very close to the wrinkle wavelength for the samples with $h = 135$ and 225 nm where the wrinkles and buckle-delaminations are coexisted. For the sample with $h = 360$ nm, however, the buckle-delaminations are dominant completely and the delamination width would be much larger than the wrinkle wavelength (see Fig. S6 in the ESI†). On the other hand, the wrinkle amplitude first increases steadily with the film thickness. When the buckle-delaminations form, the wrinkle amplitude decreases slightly. The amplitude of delaminations is much larger than that of wrinkles. For the sample with $h = 360$ nm, the delamination amplitude can be beyond 100 μm while the wrinkle amplitude decreases to nearly zero by strain localization (see Fig. S6 in the ESI†). In our experiment, the critical wrinkling strain, compressive strain (~23.1%), and material parameters of film-substrate systems are all constant. Based on eqn (3) and (5), the wrinkle wavelength is only dependent on the film thickness, *i.e.*, $\lambda \propto h$. This theoretical predication is in good agreement with the experimental measurement, as shown in Fig. 4(c). Furthermore, the wrinkle amplitude is also directly proportional to the film thickness before the formation of buckle-delaminations, as shown in Fig. 4(d).

3.4. Dependence of substrate modulus

Fig. 5(a) shows the surface morphologies of Ag film/liquid PDMS systems with different prepolymer-to-crosslinker ratios after prestrain releasing. Fig. 5(b) shows the comparison of surface profiles for different prepolymer-to-crosslinker ratios. It shows that when the ratio is less than 30 : 1, sinusoidal wrinkle profiles can be observed. When the ratio is equal to 40 : 1, however, localized surface structures appear. The *in situ* evolutions of morphologies and profiles of the Ag film with $h = 90$ nm on the liquid PDMS substrate (40 : 1) during prestrain releasing are shown in Fig. S7 in the ESI.† The cross-sectional profiles (Fig. S8 in the ESI†) show that the PDMS substrate deformed conformably with the Ag film, indicating that such localized structures are not buckle-delaminations, but are ridges. According to the morphological phase diagram,[47] the ridges have the tendency to form in the case of large modulus ratio of film to substrate. It is well known that the elastic modulus of PDMS is strongly dependent on the prepolymer-to-crosslinker ratio. When the prepolymer-to-crosslinker ratio increases, the

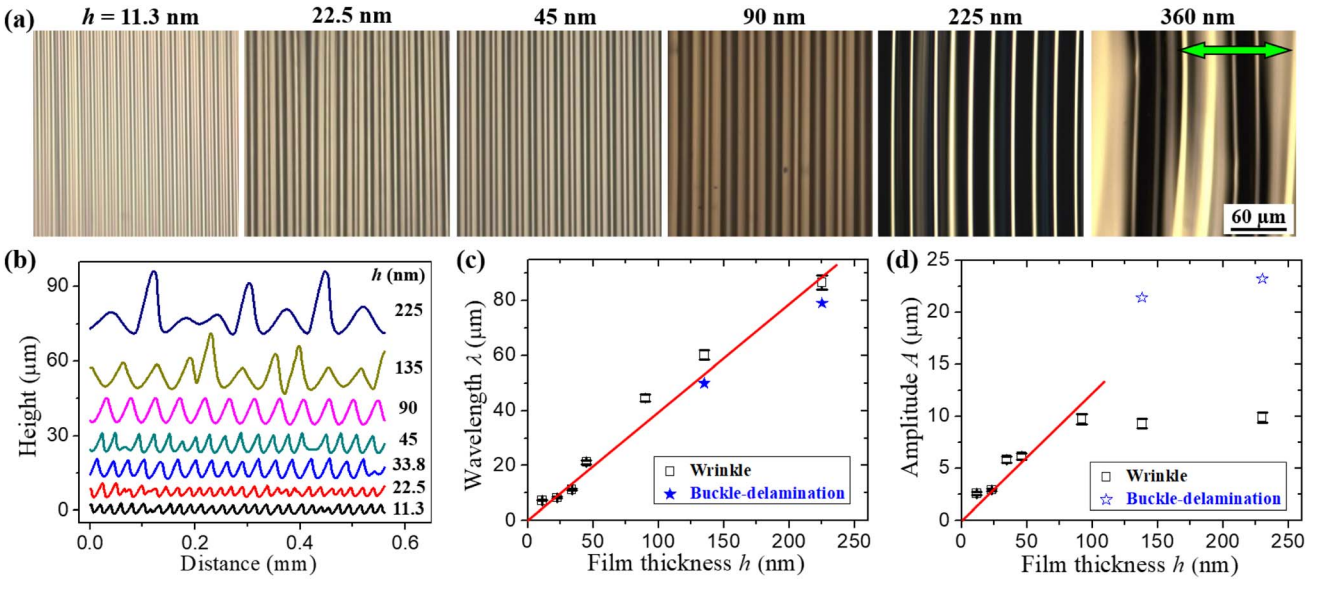

Fig. 4 (a) Surface morphologies of silver films with different thicknesses on the liquid PDMS substrates (20 : 1) after prestrain releasing (30%). (b) Surface profiles for different film thicknesses. (c and d) Evolutions of wavelength λ (c) and amplitude A (d) of wrinkles and buckle-delaminations with the film thickness h. The solid lines are linear fitting to the experimental data.

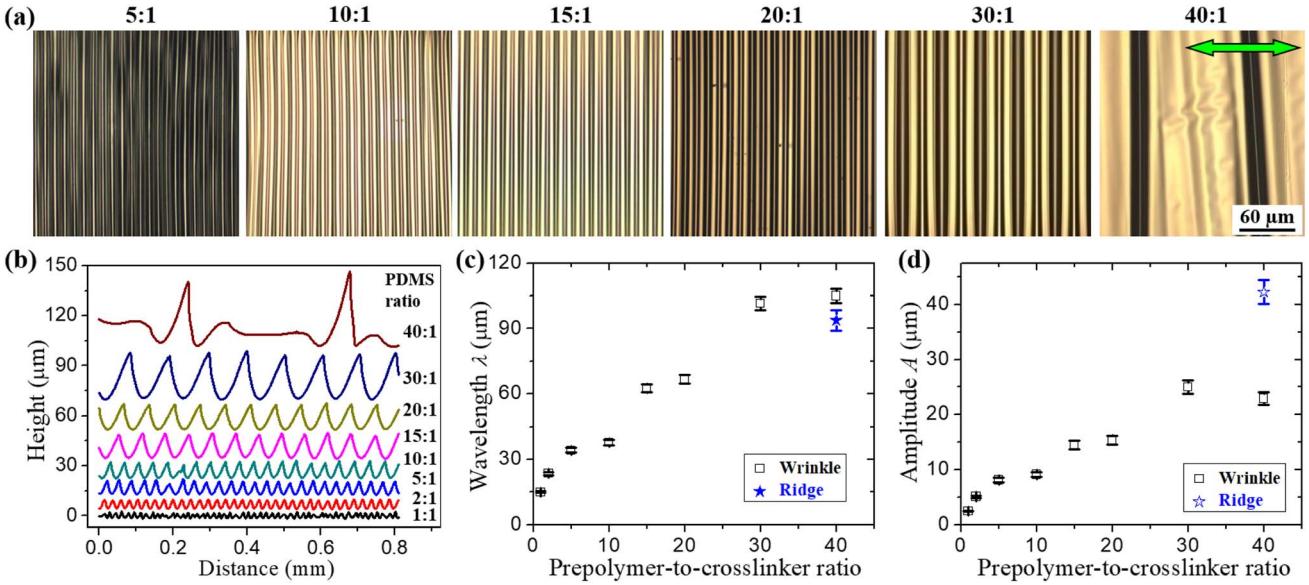

Fig. 5 (a) Surface morphologies of silver films with $h = 90$ nm on the liquid PDMS substrates with different prepolymer-to-crosslinker ratios after prestrain releasing (30%). (b) Surface profiles for different prepolymer-to-crosslinker ratios. (c and d) Evolutions of wavelength λ (c) and amplitude A (d) of wrinkles and ridges with the prepolymer-to-crosslinker ratio.

modulus of PDMS decreases greatly. The PDMS with 40 : 1 ratio is hard to be solidified due to the shortage of crosslinker. The gel-like substrate is susceptible to deforming conformably with the Ag film to generate ridge patterns under a large compressive strain.[48,49]

Fig. 5(c and d) shows the dependences of wavelengths and amplitudes of wrinkles and ridges on the prepolymer-to-crosslinker ratio. The wrinkle wavelength increases steadily with the ratio below 30 : 1, as shown in Fig. 5(c). According to eqn (3), the wrinkle wavelength is inversely proportional to the substrate modulus. Because the substrate modulus decreases with increasing prepolymer content, the wrinkle wavelength increases with the prepolymer-to-crosslinker ratio. On the other hand, the wrinkle amplitude can be expressed as $A \propto \lambda\sqrt{\varepsilon}$. For a given compressive strain, the amplitude is directly proportional to the wavelength. That is, the wrinkle amplitude has the same evolutional trend with the wrinkle wavelength, as shown in Fig. 5(d). The previous studies showed that the ridges are originated from individual wrinkle crests at high strains.[50,51] The amplitude of ridges is much larger than that of wrinkles. Furthermore, the wrinkle amplitude decreases after ridge formation due to the strain localization, as shown in Fig. 5(d). According to the finite deformation theory, the wavelength of ridges is somewhat smaller than that of wrinkles due to the larger strain in the ridge region, as shown in Fig. 5(c).

3.5. Sensing properties

The above investigations show that various surface patterns with different features and sizes can be obtained by changing film thickness, substrate modulus, and strain value. For applications as flexible strain sensors, controllable and stable surface structures under cyclic mechanical loading are required. Here we select the film thickness as 90 nm to avoid the formation of buckle-delaminations and adopt the prepolymer-to-crosslinker ratio of liquid PDMS below 30 : 1 to avoid viscoelastic behaviors of the substrate. After encapsulation, the samples are mounted onto the customized stretching devices for electrical measurements. Fig. 6(a) shows the electrical properties under strain loading for four samples: Ag films on solid PDMS (10 : 1 and 20 : 1) and liquid PDMS (10 : 1 and 20 : 1) substrates. The vertical coordinate represents relative resistance change with $\Delta R = R - R_0$, where R and R_0 are the electrical resistances at a random strain and zero strain, respectively. We find that the liquid PDMS can greatly improve the measurement range of sensors, which is defined as the strain range that the sensor can output accurate and reliable signals. The sensing range of 20 : 1 PDMS is larger than that of 10 : 1 PDMS. Furthermore, increasing prestrain can further improve the measurement range of sensors, as shown in Fig. S9 in the ESI.† For the sample prepared with 70% prestrain, the maximum sensing range can be close to 80%. Note that although the larger prestrain leads to a larger measurement range, the resistance change will be relatively small in the small strain range. It is a contradiction between large sensing range and high sensitivity for strain sensors.

It is well known that the slope of electrical resistance curve characterizes the gauge factor (GF) of sensors, which is expressed as

$$\sigma_{GF} = \frac{(R - R_0)/R_0}{\varepsilon} = \frac{\Delta R/R_0}{\varepsilon}. \quad (7)$$

Fig. 6(a) shows that the electrical resistance curve for the sample of 20 : 1 liquid PDMS can be roughly divided into three ranges according to the slope change: GF = 45.6 for 0–28%, GF = 1302 for 28–32%, GF = 4125 for 32–36%. For the range far

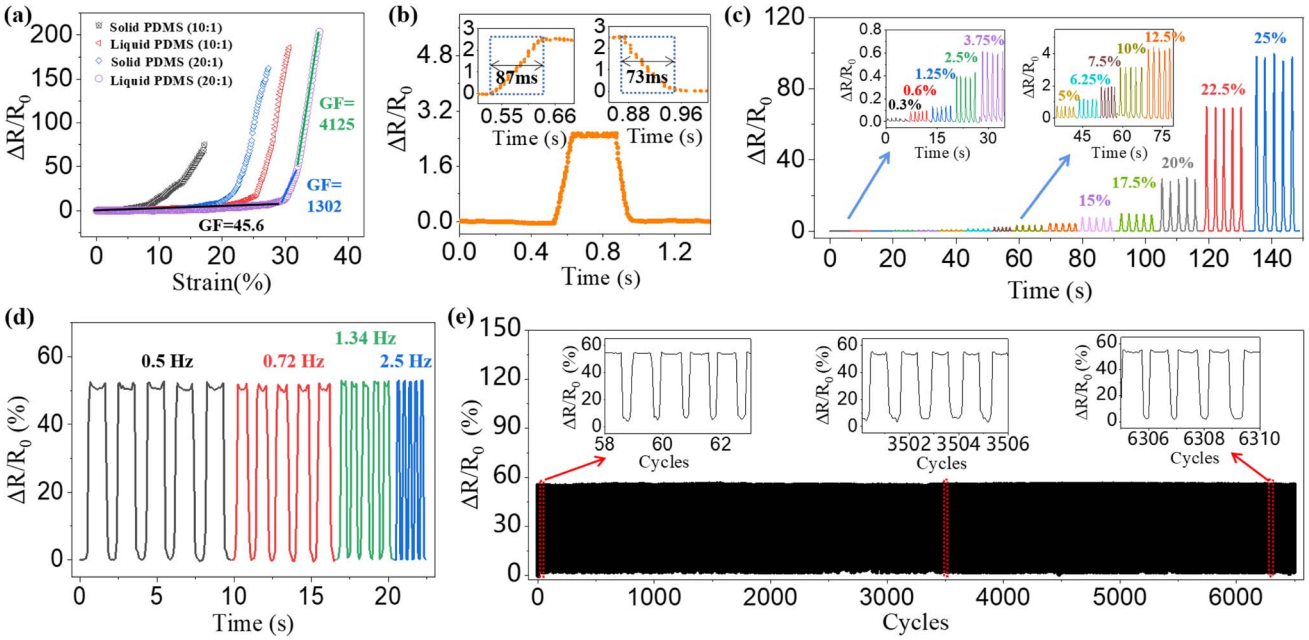

Fig. 6 Sensor properties based on the Ag film/liquid PDMS systems with 30% prestrain. (a) Relative electrical resistance variation under strain loading for the Ag films on solid PDMS (10 : 1 and 20 : 1) and liquid PDMS (10 : 1 and 20 : 1) substrates. (b) Response and relaxation behaviors under 10% strain loading and unloading. (c) Cyclic stretching/releasing test at different strain levels. (d) Cyclic stretching/releasing test at different loading frequencies. (e) Durability of the strain sensor under more than 6000 cycles at 2.5% strain.

below the prestrain, the strain is released by flattening of wrinkled surface and the Ag film keeps intact. When the strain approaches to or slightly exceeds the prestrain (30%), microcracks form in the film, leading to the quick rise of the electrical resistance. Finally, macro cracks start to propagate in the film, forming channel cracks and blocking the electrical path, as shown in Fig. S10 in the ESI.† The response speed is also an important criterion for flexible strain sensors. Fig. 6(b) shows the response of electrical resistance for loading and unloading of 10% strain. The response time (strain loading) and relaxation time (strain unloading) are about 87 ms and 73 ms, respectively. This exhibits the quick response of the sensors based on Ag film/liquid PDMS systems.

To verify the dynamic response of the sensors at different strain levels, we have performed the stretching/releasing test in the strain range of 0–25%, as shown in Fig. 6(c). A good stability and reliability can be observed within the entire strain range. We also performed the stretching/releasing test at different loading frequencies, as shown in Fig. 6(d). It is clear that the sensing properties are almost independent of the loading frequency, showing a good response characteristics. Furthermore, the durability is an important factor for practical applications of flexible strain sensors. We have performed the stretching/releasing test at 2.5% strain for more than 6000 cycles, as shown in Fig. 6(e). The insets show the electrical resistance curves in the early, middle and late stages. It is clear that the electrical resistance curves have no obvious change and the sensing properties keep stable during the entire process. Fig. S11 in the ESI† shows that the morphologies and profiles of the wrinkles are almost unchanged during the cycling process. In comparison, the surface morphologies and profiles of the Ag film/solid PDMS system change greatly and buckle delaminations form only after 500 cycles at 5% strain, as shown in Fig. S12 in the ESI.† As a result, the electrical resistance curves become much chaotic during the cycling process, as shown in Fig. S13 in the ESI.† These results demonstrate that the sensors based on the Ag film/liquid PDMS system possess a good durability and long serving life, far superior to the sensors based on the Ag film/solid PDMS system. The improvement of the stability and durability for liquid PDMS case is attributed to the formation of an interlocking layer and enhancement of interfacial adhesion.

3.6. Practical application

The flexible strain sensors can be applied to detect the human motions including the strong physical motion and weak physiological signal. We first attach the sensor on the joint of an index finger. When the index finger bends to different angles (about 30°, 60° and 90°), the sensor responds to the motion quickly and exhibits different electrical signals at different bending angles, as shown in Fig. 7(a). When the sensor is attached to the Adam's apple of a volunteer, it can detect the swallowing behavior. Because the Adam's apple first moves upward and then moves downward during the swallowing process, double-humped characteristic can be observed on the electrical resistance curve, as shown in Fig. 7(b). When the sensor is attached to the wrist of a volunteer, the electrical resistance response exhibits a main peak and an accompanying peak by wrist bending, as shown in Fig. 7(c). The main peak is caused by the contraction of the flexor carpi radialis tendon during bending. When the wrist flattens, the palmaris longus

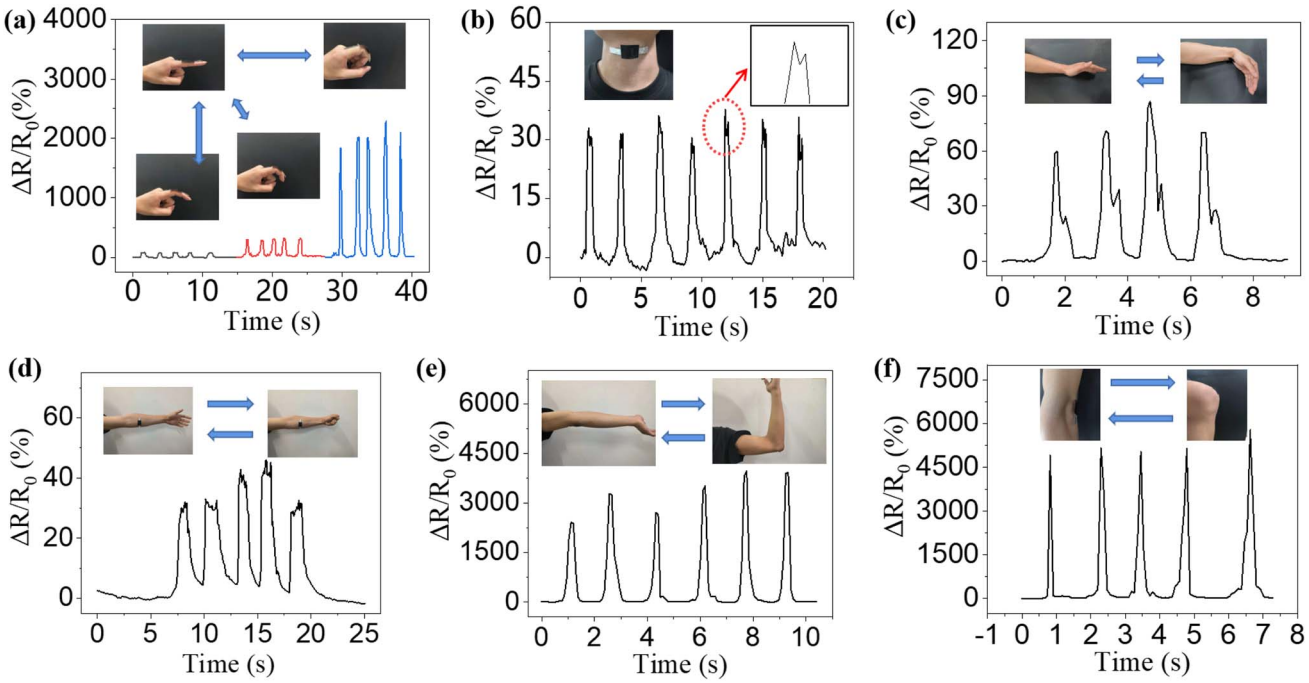

Fig. 7 Practical applications of the flexible strain sensors. (a) Electrical resistance variation by bending the index finger for different angles (about 30°, 60° and 90°). (b) Electrical resistance variation by swallowing. (c) Electrical resistance variation by bending the wrist. (d) Electrical resistance variation by making a fist. (e) Electrical resistance variation by bending the upper arm. (f) Electrical resistance variation by standing and sitting down.

tendon contracts to control the motion of fingers, leading to the formation of the accompanying peak. Similarly, when the sensor is attached to the arm of a volunteer, it can detect the relaxation and tension of the arm, as shown in Fig. 7(d). Furthermore, the sensor can well detect the human motions under large strains. For examples, when the sensor is attached to the elbow joint or knee joint, the bending of elbow or knee demonstrates a quick and stable electrical response, as shown in Fig. 7(e and f).

4. Conclusions

In summary, flexible strain sensors based on controllable silver film wrinkles modulated by liquid PDMS are described and discussed in detail. It is found that the surface morphologies of silver films on the liquid PDMS substrates are strongly dependent on the film thickness, prepolymer-to-crosslinker ratio of PDMS, and strain value. The *in situ* research shows that the wrinkle wavelength decreases while the amplitude increases steadily during the prestrain releasing process, in good agreement with the predication of the finite deformation theory. The wrinkle wavelength and amplitude increase linearly with the film thickness, whereas buckle delaminations form for thicker films. The wrinkle wavelength and amplitude also increase with the prepolymer-to-crosslinker ratio of PDMS, while ridge patterns form for the sample of 40 : 1 PDMS. By comparing the samples prepared on the liquid and solid PDMS substrates, it shows that the using of liquid PDMS enhances the interfacial adhesion, alleviates the crack formation, and stabilizes the film microstructure significantly. As a result, the flexible strain sensors based on the silver film/liquid PDMS system show high comprehensive performances, including high sensitivity (above 4000), wide sensing range (~80%, depending on the prestrain), quick response speed (~80 ms), and good stability (above 6000 cycles). This work provides a deep insight into the modulation effect of liquid PDMS on the interfacial characteristic and mechanical response of film-substrate systems. The flexible strain sensors prepared by using liquid PDMS have a broad application prospect in the fields of health monitoring, motion tracking, and human–machine interaction.

Author contributions

Yifan Xu performed the experiments and characterization, analyzed the data and wrote the manuscript. Miaogen Chen provided helpful discussions and reviewed the manuscript. Senjiang Yu analyzed the data and wrote the manuscript. Hong Zhou performed the experiments and characterization. All authors have given approval to the final version of the manuscript.

Conflicts of interest

The authors declare no conflict of interest.

Acknowledgements

The authors acknowledge the support from the National Key R&D Program of China (No. 2019YFE0112000), the Natural Science Foundation of Zhejiang Province (No. LZ23A020003),

the National Natural Science Foundation of China (No. 12172113) and the Fundamental Research Funds for the Provincial Universities of Zhejiang (No. 2021YW25).

References

1 A. Moin, A. Zhou, A. Rahimi, A. Menon, S. Benatti, G. Alexandrov, S. Tamakloe, J. Ting, N. Yamamoto, Y. Khan, F. Burghardt, L. Benini, A. C. Arias and J. M. Rabaey, A wearable biosensing system with in-sensor adaptive machine learning for hand gesture recognition, *Nat. Electron.*, 2021, **4**, 54–63.

2 S. Zhang, S. Li, Z. Xia and K. Cai, A review of electronic skin: Soft electronics and sensors for human health, *J. Mater. Chem. B*, 2020, **8**, 852–862.

3 X. Dong, X. Luo, H. Zhao, C. Qiao, J. Li, J. Yi, L. Yang, F. J. Oropeza, T. S. Hu, Q. Xu and H. Zeng, Recent advances in biomimetic soft robotics: fabrication approaches, driven strategies and applications, *Soft Matter*, 2022, **18**, 7699–7734.

4 T. Cao, X.-L. Shi, J. Zou and Z.-G. Chen, Advances in conducting polymer-based thermoelectric materials and devices, *Microstructures*, 2021, **1**, 2021007.

5 S. Wang, J. Xu, W. Wang, G. J. N. Wang, R. Rastak, F. Molina-Lopez, J. W. Chung, S. Niu, V. R. Feig, J. Lopez, T. Lei, S. K. Kwon, Y. Kim, A. M. Foudeh, A. Ehrlich, A. Gasperini, Y. Yun, B. Murmann, J. B. H. Tok and Z. Bao, Skin electronics from scalable fabrication of an intrinsically stretchable transistor array, *Nature*, 2018, **555**, 83–88.

6 Y. Qiu, Z. Wang, P. Zhu, B. Su, C. Wei, Y. Tian, Z. Zhang, H. Chai, A. Liu, L. Liang and H. Wu, A multisensory-feedback tactile glove with dense coverage of sensing arrays for object recognition, *Chem. Eng. J.*, 2023, **455**, 140890.

7 P. Won, K. K. Kim, H. Kim, J. J. Park, I. Ha, J. Shin, J. Jung, H. Cho, J. Kwon, H. Lee and S. H. Ko, Transparent soft actuators/sensors and camouflage skins for imperceptible soft robotics, *Adv. Mater.*, 2021, **33**, 2002397.

8 D. G. Mackanic, T. H. Chang, Z. Huang, Y. Cui and Z. Bao, Stretchable electrochemical energy storage devices, *Chem. Soc. Rev.*, 2020, **49**, 4466–4495.

9 Y. Ma, Y. Zhang, S. Cai, Z. Han, X. Liu, F. Wang, Y. Cao, Z. Wang, H. Li, Y. Chen and X. Feng, Flexible hybrid electronics for digital healthcare, *Adv. Mater.*, 2020, **32**, 1902062.

10 W. Zhang, L. Xu, M. Zhao, Y. Ma, T. Zheng and L. Shi, Stretchable, self-healing and adhesive sodium alginate-based composite hydrogels as wearable strain sensors for expansion–contraction motion monitoring, *Soft Matter*, 2022, **18**, 1644–1652.

11 R. Nur, N. Matsuhisa, Z. Jiang, M. O. G. Nayeem, T. Yokota and T. Someya, A highly sensitive capacitive-type strain sensor using wrinkled ultrathin gold films, *Nano Lett.*, 2018, **18**, 5610–5617.

12 H. Zhang, W. Han, K. Xu, Y. Zhang, Y. Lu, Z. Nie, Y. Du, J. Zhu and W. Huang, Metallic sandwiched-aerogel hybrids enabling flexible and stretchable intelligent sensor, *Nano Lett.*, 2020, **20**, 3449–3458.

13 Z. Shen, Z. Zhang, N. Zhang, J. Li, P. Zhou, F. Hu, Y. Rong, B. Lu and G. Gu, High-stretchability, ultralow-hysteresis conducting polymer hydrogel strain sensors for soft machines, *Adv. Mater.*, 2022, **34**, 2203650.

14 W. Fan, Q. He, K. Meng, X. Tan, Z. Zhou, G. Zhang, J. Yang and Z. L. Wang, Machine-knitted washable sensor array textile for precise epidermal physiological signal monitoring, *Sci. Adv.*, 2020, **6**, eaay2840.

15 R. Li, J. Ren, M. Li, M. Zhang, Y. Li and W. Yang, Self-healing, self-adhesive, stretchable and flexible conductive hydrogels for high-performance strain sensors, *Soft Matter*, 2023, **19**, 5723–5736.

16 H. Souri, H. Banerjee, A. Jusufi, N. Radacsi, A. A. Stokes, I. Park, M. Sitti and M. Amjadi, Wearable and stretchable strain sensors: materials, sensing mechanisms, and applications, *Adv. Intell. Syst.*, 2020, **2**, 2000039.

17 J. Zhou, X. Long, J. Huang, C. Jiang, F. Zhuo, C. Guo, H. Li, Y. Q. Fu and H. Duan, Multiscale and hierarchical wrinkle enhanced graphene/Ecoflex sensors integrated with human-machine interfaces and cloud-platform, *npj Flexible Electron.*, 2022, **6**, 55.

18 R. Yin, D. Wang, S. Zhao, Z. Lou and G. Shen, Wearable sensors-enabled human-machine interaction systems: from design to application, *Adv. Funct. Mater.*, 2021, **31**, 2008936.

19 D. Kang, P. V. Pikhitsa, Y. W. Choi, C. Lee, S. S. Shin, L. Piao, B. Park, K. Y. Suh, T. Kim and M. Choi, Ultrasensitive mechanical crack-based sensor inspired by the spider sensory system, *Nature*, 2014, **516**, 222–226.

20 A. Miyamoto, S. Lee, N. F. Cooray, S. Lee, M. Mori, N. Matsuhisa, H. Jin, L. Yoda, T. Yokota, A. Itoh, M. Sekino, H. Kawasaki, T. Ebihara, M. Amagai and T. Someya, Inflammation-free, gas-permeable, lightweight, stretchable on-skin electronics with nanomeshes, *Nat. Nanotechnol.*, 2017, **12**, 907–913.

21 J. Ji, C. Zhang, S. Yang, Y. Liu, J. Wang and Z. Shi, High sensitivity and a wide sensing range flexible strain sensor based on the V-groove/wrinkles hierarchical array, *ACS Appl. Mater. Interfaces*, 2022, **14**, 24059–24066.

22 Y. Wu, K. Schlingman, S. S. Mechael, Y. Chen and T. B. Carmichael, Engineering the cracking patterns in stretchable copper films using acid-oxidized poly (dimethylsiloxane) substrates, *ACS Appl. Electron. Mater.*, 2022, **4**, 5565–5572.

23 Z. Chu, W. Jiao, J. Li, H. Guo, Y. Zheng, R. Wang and X. He, A novel wrinkle-gradient strain sensor with anti-water interference and high sensing performance, *Chem. Eng. J.*, 2021, **421**, 129873.

24 L. Li, Y. Zheng, E. Liu, J. Wang, X. Han, S. Jiang, F. Xu and C. Lu, Ultrafast dynamic response of waterproof stretchable strain sensors based on wrinkle-templated microcracking, *J. Mater. Chem. A*, 2022, **10**, 16297–16308.

25 G. Lee, G. Y. Bae, J. H. Son, S. Lee, S. W. Kim, D. Kim, S. G. Lee and K. Cho, User-interactive thermotherapeutic electronic skin based on stretchable thermochromic strain sensor, *Adv. Sci.*, 2020, **7**, 2001184.

26 W. Peng, L. Han, H. Huang, X. Xuan, G. Pan, L. Wan, T. Lu, M. Xu and L. Pan, A direction-aware and ultrafast self-healing dual network hydrogel for a flexible electronic skin strain sensor, *J. Mater. Chem. A*, 2020, **8**, 26109–26118.

27 X. Xiao, L. Yuan, J. Zhong, T. Ding, Y. Liu, Z. Cai, Y. Rong, H. Han, J. Zhou and Z. L. Wang, High-strain sensors based on ZnO nanowire/polystyrene hybridized flexible films, *Adv. Mater.*, 2011, **23**, 5440–5444.

28 Q. Zhang, Y. Tang, M. Hajfathalian, C. Chen, K. T. Turner, D. A. Dikin, G. Lin and J. Yin, Spontaneous periodic delamination of thin films to form crack-free metal and silicon ribbons with high stretchability, *ACS Appl. Mater. Interfaces*, 2017, **9**, 44938–44947.

29 S. Wu, S. Yao, Y. Liu, X. Hu, H. H. Huang and Y. Zhu, Buckle-delamination-enabled stretchable silver nanowire conductors, *ACS Appl. Mater. Interfaces*, 2020, **12**, 41696–41703.

30 Z. Chen, B. Cotterell, W. Wang, E. Guenther and S. J. Chua, A mechanical assessment of flexible optoelectronic devices, *Thin Solid Films*, 2001, **394**, 201–205.

31 Y. Yu, F. Xie, X. Gao and L. Zheng, Double-network hydrogels with adjustable surface morphology and multifunctional integration for flexible strain sensors, *Soft Matter*, 2021, **17**, 4352–4362.

32 T. Zhu, K. Wu, Y. Xia, C. Yang, J. Chen, Y. Wang, J. Zhang, X. Pu, G. Liu and J. Sun, Topological gradients for metal film-based strain sensors, *Nano Lett.*, 2022, **22**, 6637–6646.

33 J. Wang, L. Liu, C. Yang, C. Zhang, B. Li, X. Meng, G. Ma, D. Wang, J. Zhang, S. Niu, J. Zhao, Z. Han, Z. Yao and L. Ren, Ultrasensitive, highly stable, and flexible strain sensor inspired by nature, *ACS Appl. Mater. Interfaces*, 2022, **14**, 16885–16893.

34 S. Yu, Y. Sun, S. Li and Y. Ni, Harnessing fold-to-wrinkle transition and hierarchical wrinkling on soft material surfaces by regulating substrate stiffness and sputtering flux, *Soft Matter*, 2018, **14**, 6745–6755.

35 Z. Liu, H. Wang, P. Huang, J. Huang, Y. Zhang, Y. Wang, M. Yu, S. Chen, D. Qi, T. Wang, Y. Jiang, G. Chen, G. Hu, W. Li, J. Yu, Y. Luo, X. J. Loh, B. Liedberg, G. Li and X. Chen, Highly stable and stretchable conductive films through thermal-radiation-assisted metal encapsulation, *Adv. Mater.*, 2019, **31**, 1901360.

36 D. Rhee, W. K. Lee and T. W. Odom, Crack-Free, soft wrinkles enable switchable anisotropic wetting, *Angew. Chem., Int. Ed.*, 2017, **129**, 6623–6627.

37 J. Marthelot, B. Roman, J. Bico, J. Teisseire, D. Dalmas and F. Melo, Self-replicating cracks: a collaborative fracture mode in thin films, *Phys. Rev. Lett.*, 2014, **113**, 085502.

38 E. J. Kappert, D. Pavlenko, J. Malzbender, A. Nijmeijer, N. E. Benes and P. A. Tsai, Formation and prevention of fractures in sol–gel-derived thin films, *Soft Matter*, 2015, **11**, 882–888.

39 A. L. Volynskii, S. Bazhenov, O. V. Lebedeva, A. N. Ozerin and N. F. Bakeev, Multiple cracking of rigid platinum film covering polymer substrate, *J. Appl. Polym. Sci.*, 1999, **72**, 1267–1275.

40 N. Bowden, S. Brittain, A. G. Evans, J. W. Hutchinson and G. M. Whitesides, Spontaneous formation of ordered structures in thin films of metals supported on an elastomeric polymer, *Nature*, 1998, **393**, 146–149.

41 S. Yu, X. Zhang, X. Xiao, H. Zhou and M. Chen, Wrinkled stripes localized by cracks in metal films deposited on soft substrates, *Soft Matter*, 2015, **11**, 2203–2212.

42 E. Cerda and L. Mahadevan, Geometry and physics of wrinkling, *Phys. Rev. Lett.*, 2003, **90**, 074302.

43 H. Jiang, D. Y. Khang, J. Song, Y. Sun, Y. Huang and J. A. Rogers, Finite deformation mechanics in buckled thin films on compliant supports, *Proc. Natl. Acad. Sci. U. S. A.*, 2007, **104**, 15607–15612.

44 H. Mei, C. M. Landis and R. Huang, Concomitant wrinkling and buckle-delamination of elastic thin films on compliant substrates, *Mech. Mater.*, 2011, **43**, 627–642.

45 K. Pan, Y. Ni, L. He and R. Huang, Nonlinear analysis of compressed elastic thin films on elastic substrates: From wrinkling to buckle-delamination, *Int. J. Solids Struct.*, 2014, **51**, 3715–3726.

46 A. J. Nolte, J. Y. Chung, C. S. Davis and C. M. Stafford, Wrinkling-to-delamination transition in thin polymer films on compliant substrates, *Soft Matter*, 2017, **13**, 7930–7937.

47 H. Son, A. L. Chau and C. S. Davis, Polymer thin film adhesion utilizing the transition from surface wrinkling to delamination, *Soft Matter*, 2019, **15**, 6375–6382.

48 Q. Wang and X. Zhao, A three-dimensional phase diagram of growth-induced surface instabilities, *Sci. Rep.*, 2015, **5**, 8887.

49 Z. Cheng and F. Xu, Intricate evolutions of multiple-period post-buckling patterns in bilayers, *Sci. China: Phys., Mech.*, 2021, **64**, 214611.

50 J. Zang, X. Zhao, Y. Cao and J. W. Hutchinson, Localized ridge wrinkling of stiff films on compliant substrates, *J. Mech. Phys. Solids*, 2012, **60**, 1265–1279.

51 L. Jin, A. Takei and J. W. Hutchinson, Mechanics of wrinkle/ridge transitions in thin film/substrate systems, *J. Mech. Phys. Solids*, 2015, **81**, 22–40.